Paramagnetic ^{7}Li NMR Shifts and Magnetic Properties of Divalent Transition Metal Silylamide Ate Complexes [LiM{N(SiMe$_3$)$_2$}$_3$] (M^{2+} = Mn, Fe, Co)

Sylvio Indris, Thomas Bredow, Björn Schwarz, and Andreas Eichhöfer*

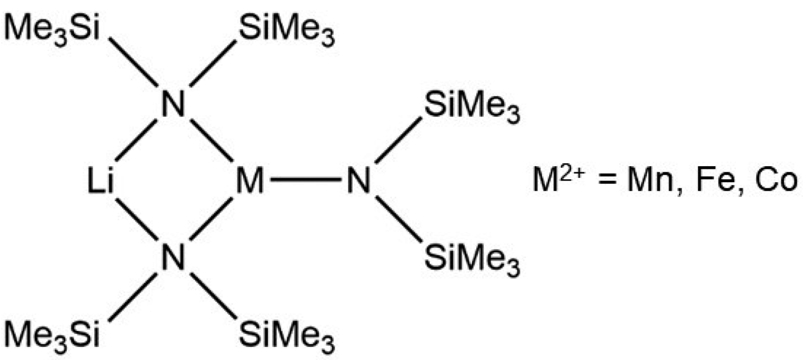

ABSTRACT: ^{7}Li NMR shifts and magnetic properties have been determined for three so-called ate complexes [LiM{N(SiMe$_3$)$_2$}$_3$] (M^{2+} = Mn, Fe, Co; e.g., named lithium-tris(bis(trimethylsilylamide))-manganate(II) in accordance with a formally negative charge assigned to the complex fragment [M{N(SiMe$_3$)$_2$}$_3$]$^-$, which comprises the transition metal). They are formed by addition reactions of LiN(SiMe$_3$)$_2$ and [M{N(SiMe$_3$)$_2$}$_2$] and stabilized by Lewis base/Lewis acid interactions. The results are compared to those of the related "ion-separated" complexes [Li(15-crown-5)][M{N(SiMe$_3$)$_2$}$_3$]. The ate complexes with the lithium atoms connected to the 3d metal atoms manganese, iron, or cobalt via μ_2 nitrogen bridges reveal strong ^{7}Li NMR paramagnetic shifts of about −75, 125, and 171 ppm, respectively, whereas the shifts for the lithium ions coordinated by the 15-crown-5 ether are close to zero. The observed trends of the ^{7}Li NMR shifts are confirmed by density-functional theory calculations. The magnetic dc and ac properties display distinct differences for the six compounds under investigation. Both manganese compounds, [LiMn{N(SiMe$_3$)$_2$}$_3$] and [Li(15-crown-5)][Mn{N(SiMe$_3$)$_2$}$_3$], display almost pure and ideal spin-only paramagnetic behavior of a 3d^5 high-spin complex. In this respect slightly unexpected, both complexes show slow relaxation behavior at low temperatures under applied dc fields, which is especially pronounced for the ate complex [LiMn{N(SiMe$_3$)$_2$}$_3$]. Dc magnetic properties of the iron complexes reveal moderate *g*-factor anisotropies with small values of the axial magnetic anisotropy parameter *D* and a larger *E* (transversal anisotropy). Both complexes display at low temperatures and, under external dc fields of up to 5000 Oe, only weak ac signals with no maxima in the frequency range from 1 to 1500 s^{-1}. In contrast, the two cobalt complexes display strong *g*-factor anisotropies with large values of *D* and *E*. In addition, in both cases, the ac measurements at low temperatures and applied dc fields reveal two, in terms of their frequency range, well separated relaxation processes with maxima lying for the most part outside of the measurement range between 1 and 1500 s^{-1}.

■ INTRODUCTION

Low coordinated bis(trimethylsilyl)amido complexes of first row transition metals [M{N(SiMe$_3$)$_3$}$_n$] (n = 2, 3) and related heteroleptic compounds are interesting research objects in coordination chemistry.[1−4] Their discovery is based on the pioneering work of Bürger and Wannagat[5,6] as well as Bradley et al.,[7−11] being further developed, among others,[12,13] by Power and co-workers.[1,4,14−16]

Recently, this class of compounds gained new interest concerning investigations related to single-ion magnetic behavior, a phenomenon which may in the future enable the utilization of such and related molecules as the smallest possible units in spin-based computational or data storage devices.[17] Most prominent examples among the bis(trimethylsilyl)amido complexes are two coordinate complexes such as [$Fe\{N(SiMe_3)(Dipp)\}_2$] (dipp = C_6H_3-2,6-$^iPr_2$).[18,19] But also three coordinate iron(II/III), cobalt(II), and nickel(I) complexes, i.e., [$M\{N(SiMe_3)_3\}_2L$] (M = Fe, Co; L = ligand),[20−23] [$Fe\{N(SiMe_3)_3\}_3$],[24,25] and [$Ni(N(SiMe_3)_2)(PPh_3)_2$][26] and four-coordinate chromium(II) complexes [$Cr(N(SiMe_3)_2)_2(L)_2$] (L = py, thf) attracted some attention.[27] One further important aspect is studies of the coordination behavior of these coordinatively unsaturated compounds, a situation which also enables them to activate small molecules.[28−31] Finally, basic aspects like optimization of existing synthetic protocols including the synthesis of new compounds are still an actual and common interest like evidenced by some recent papers.[32−36]

A special class of compounds therein are so-called ate complexes in which an alkali metal ion (Li, Na, K) is directly connected through bridging silylamido ligands with a 3d metal ion (Cr, Mn, Fe, Co; Figure 1). They can be synthesized by reaction of $M'N(SiMe_3)_2$ (M′ = alkali metal Li, Na, K) with dimeric bis(trimethylsilyl)amido complexes of manganese, iron, and cobalt [$M\{N(SiMe_3)_2\}_2$]$_2$ (M = Mn, Fe, Co) and are stabilized by Lewis acid/base interactions. Known examples include the complexes [$(thf)LiMn\{N(SiMe_3)_2\}_3$],[14] [$(thf)NaM\{N(SiMe_3)_2\}_3$] (M = Cr,[37] Fe,[38] Co[37]), and "solvent-free" [$LiFe\{N(SiMe_3)_2\}_3$].[37]

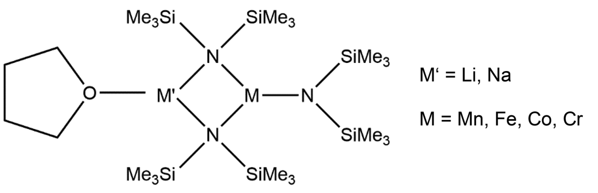

Figure 1. Schematic structure of transition metal bis(trimethylsilylamido) ate complexes.

Solid-state nuclear magnetic resonance (NMR) spectroscopy is a widespread tool to investigate element-specifically local environments and structural building units in crystalline or amorphous solids. The relatively new field of paramagnetic NMR spectroscopy makes use of a specific interaction of the probe nuclei with unpaired electron spin density from neighboring elements such as transition metals.[39] One example is ^1H NMR investigations on organic transition metal complexes.[40,41] Another prominent topic is NMR investigations on battery materials,[42,43] specifically cathode materials, that contain paramagnetic transition metals as well as diamagnetic NMR-active nuclei, e.g., ^7Li. In this case, electron spin density is transferred from the transition metal elements via oxygen bonds to lithium, resulting in large NMR shifts of up to several hundred or thousand parts per million (ppm), which contrast the smaller NMR shifts usually observed for diamagnetic compounds. Some examples include $^6Li/^7Li$ NMR investigations on layered lithium transition metal oxides[42−44] and lithium transition metal phosphates[44−48] as well as ^{23}Na NMR on Na_2FePO_4F.[49] ^7Li NMR has recently also been used as a probe to investigate ate complexes of paramagnetic cerium silylamides[50] or to better understand reagents used in organic synthesis.[51]

In the current study, we report on ^7Li magic-angle spinning (MAS) NMR investigations and magnetic studies on three "ate complexes" [$LiM\{N(SiMe_3)_2\}_3$] (M = Mn^{2+}, Fe^{2+}, Co^{2+}) in comparison to the related "ion-free" compounds [Li(15-crown-5)][$M\{N(SiMe_3)_2\}_3$]. The measured trends of the paramagnetic shifts of the ate complexes are supported by quantum chemical calculations.

RESULTS AND DISCUSSION

Synthesis, Structure, and Optical Spectroscopy. The complexes [$LiM\{N(SiMe_3)_2\}_3$] (M = Mn (**1**), Fe (**2**), Co (**3**)) were synthesized by the reaction of [$M\{N(SiMe_3)_2\}_2$]$_2$ (M = Mn,[52] Fe,[32] Co[53]) with lithium bis(trimethylsilyl)amide as reported before for the iron complex (Scheme 1).[37]

Scheme 1. Synthesis Reactions for 1−3

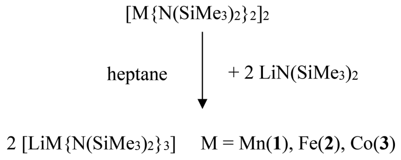

In similar reactions, the complexes [Li(15-crown-5)][$M\{N(SiMe_3)_2\}_3$] (M = Mn (**4**), Fe (**5**), Co (**6**)) were synthesized by the addition of 15-crown-5 to the reaction solutions as reported for the iron and cobalt complex before.[21]

Crystal structures have been determined for the new complexes **1**, **3**, and **4** (Table S1, in the Supporting Information (SI)). The manganese complex **1** crystallizes in the triclinic space group $P\bar{1}$, whereas the cobalt complex **3** with the same composition and molecular structure crystallizes in $P2_1/n$ similar to the related iron compound **2** (Figures 2 and 3 and Figure S1 in the SI).[37] The transition metal centers reveal a distorted trigonal-planar coordination by three $-N(SiMe_3)_2$ ligands comprising two larger N−M−N angles (M = Mn: 132.0, 132.8°; M = Co: 128.8, 131.0°) and one smaller (M = Mn: 95.2; M = Co: 99.9°) (for bond lengths and angles, see Table 1). The latter one is formed by the two nitrogen atoms from the $-N(SiMe_3)_2$ groups which build the μ_2 bridges to the lithium atom with M−N−Li angles ranging in **1** and **3** from 78.2 to 80.1°. M−N bond distances are by approximately 10 pm longer for the bridging groups than for the terminal ligand. Nonbonding M···Li distances amount to 262.4 in **1** and 259.6 pm in **3**.

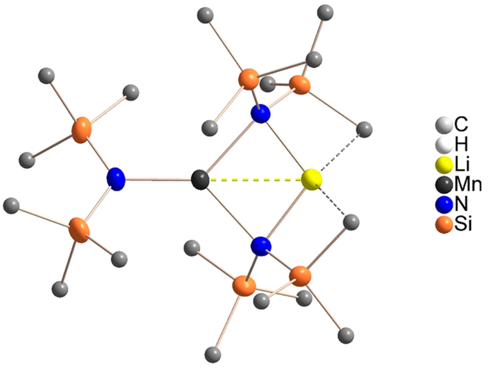

Figure 2. Molecular structure of [$LiMn\{N(SiMe_3)_2\}_3$] (**1**; H atoms are omitted for clarity). Thermal ellipsoid plots at 50% probability. For selected bond lengths and angles, see Table 1.

The ionic complex **4** crystallizes in the monoclinic space group $P2_1/n$ (Table S1) with one toluene molecule in the asymmetric unit similar to the isostructural complexes **5** and **6**.[21] The cations are built by dimerization of two [Li(15-crown-5)]$^+$ units, with the lithium atoms separated by a shortest

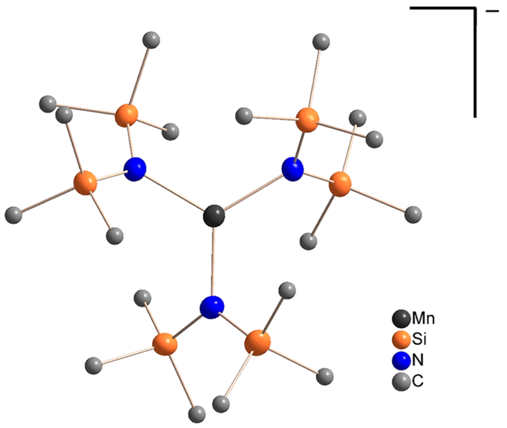

Figure 3. Molecular structure of the anion $[Mn\{N(SiMe_3)_2\}_3]^-$ in **4** (H atoms are omitted for clarity). Thermal ellipsoid plots at 50% probability. For selected bond lengths and angles, see Table 1.

distance of 834.4 pm from the manganese atom. In the monomeric anion $[Mn\{N(SiMe_3)_2)_3]^-$, the metal ion is planary coordinated by the three nitrogen atoms of the bis(trimethylsilyl)amido groups (Figure 3). The symmetry of the complexes is only slightly distorted from an idealized D_3 point group symmetry (for bond distances and angles, see Table 1).

The measured powder X-ray diffraction (XRD) patterns of **1**, **3**, and **4** show a good agreement with the calculated ones based on the single crystal data (Figures S2−S4, SI) taking into account that the quality of the pattern of **4** suffers from the loss of toluene solvent molecules upon drying of the powder. Slightly increasing differences in the position of the peaks with increasing detection angle arise from the temperature difference between data collections (single crystal XRD at 180 K vs powder XRD at room temperature).

However, in combination with the results from C, H, and N elemental analysis, this proves the purity of the samples used for NMR spectroscopy and magnetic measurements.

UV−vis. Electronic spectra of **1**−**4** have been measured in a region from 4.0 to 0.5 eV (310−2480 nm) in C_6D_6 solution and as polycrystalline powders between two quartz plates (Figure 4 and Figures S5 and S6, SI).

For the manganese complex **1**, one observes below 4 eV (above 310 nm) three bands of low intensity ($\varepsilon < 30$ l mol^{-1} cm^{-1}) at 3.24 eV (383 nm), 2.60 eV (477 nm), and 2.10 eV (590 nm), which are more pronounced in the solid state spectrum and can be assigned as spin- and Laport-forbidden d−d transitions (Figure 4). For the iron complex **2**, one observes in C_6D_6 solution at lower energies two bands at 1.37 eV (908 nm)/1.01 eV (1255 nm) and for the cobalt complex **3**, one band at 1.7 eV (700 nm) and another, a split one, around 0.85 eV (1459 nm; Figure S5). In the ideal symmetric complexes (D_{3h} point group symmetry), one would expect two d−d transitions for the iron and three d−d transitions for the cobalt complexes, respectively.[54] A lowering of the symmetry should affect a splitting of the degenerated states leading to four transitions in the iron case and six for the cobalt complexes. In accordance to calculations done on **5** and **6** and related complexes, we suggest that for the iron and cobalt complexes one only observes the high energy bands with the others occurring at energies below 0.5 eV.[21,26]

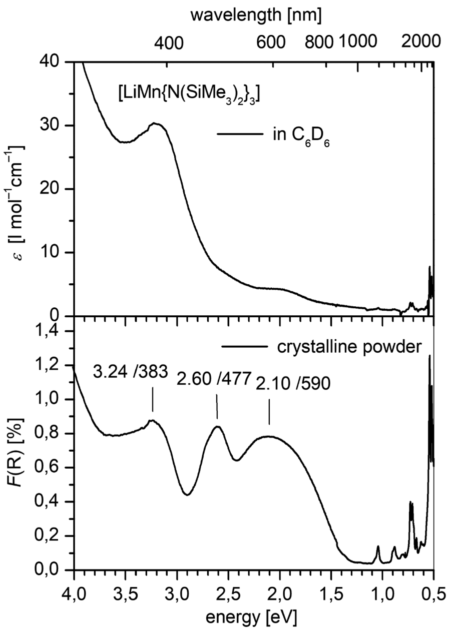

Figure 4. UV−vis NIR spectrum of **1** in C_6D_6 (up) compared to the spectrum in the solid state as microcrystalline powder in a cuvette (down).

The spectra of **4** (solution and solid state) display an almost featureless increase of the absorption intensity with no distinct bands (Figure S6).

DC Magnetic Measurements. Static (dc) and dynamic (ac) magnetic measurements were performed for **1**−**4**. Those of **5** and **6** were published before.[21] Dc magnetic data were measured between 2 and 300 K in a field of 0.1 T and magnetization measurements from 0 to 7 T at 2, 3, 4, 6, 10, and 25 K (Figures 5 and 6 and Figures S7−S10 in the SI).

The graphs of χT vs T for **1**−**6** display distinct differences due to the different electronic situation of the transition metal ions (Figures 5 and 6). Values of χT at 300 K for the manganese complexes **1** (4.843 cm^3 mol^{-1} K) and **4** (4.610 cm^3 mol^{-1} K) are slightly larger than the theoretical spin-only value of a Mn^{2+} (d^5) high spin ion (4.375 cm^3 mol^{-1} K). Upon

Table 1. Structural Parameters (Atomic Distances [pm], Bond Angles [deg]), in 1−6

	M−N	Li−N	M···Li	N−M−N	M−N−Li
1	202.4(2), 214.9(2), 216.5(2)	200.4(3), 201.1(3)	262.4(4)	95.22(6), 131.95(6), 132.83(6),	79.6(1), 80.1(1)
2[a]	192.7(1), 201.5(1), 203.4(1),	201.8(3), 205.8(3)	255.5(3)	101.38(5), 127.82(6), 130.52(6)	78.6(1), 77.3(1)
3	194.0(3), 203.8(3), 205.8(2)	202.7(6), 205.6(6)	259.6(1)	99.9(1), 128.8(1), 131.0(1)	78.2(2), 79.4(2)
4	206.8(1), 207.8(1), 206.9(1)			118.6(1), 119.3(1), 122.1(1)	
5[b]	196.9(2), 197.4(2), 197.5(2)			119.6(1), 119.6(1), 120.8(1),	
6[b]	198.4(2), 198.9(2), 198.9(2)			119.6(1), 119.8(1), 120.7(1)	

[a] Data taken from ref 37. [b] Data taken from ref 21.

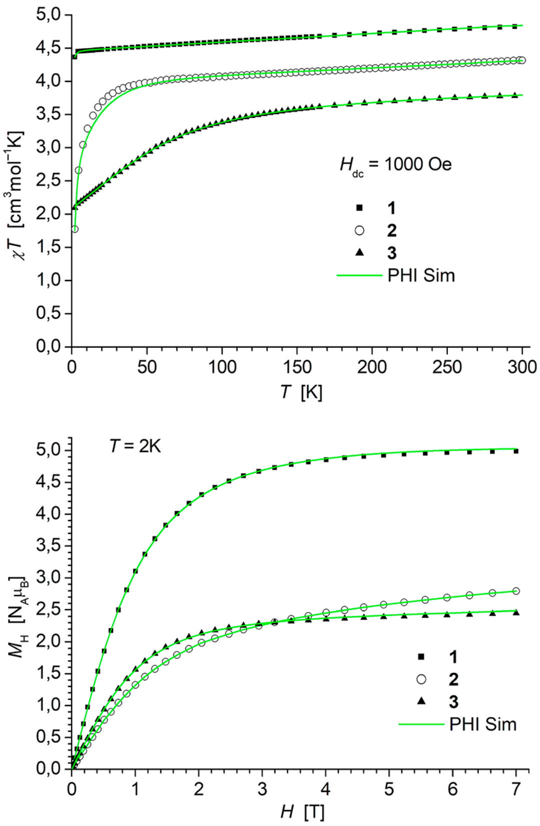

Figure 5. (a) Temperature dependence of χT and (b) plots of magnetization M versus field H at 2 K for **1**−**3**. Solid green lines represent the results of the simultaneous fittings with the temperature dependent magnetization (Table 2 and Figures S8−S10, SI) according to a spin Hamiltonian (eq S1, SI) by the PHI program.

a decrease of the temperature, the values of χT display a slight gradual decrease, which indicates the contribution of a temperature independent paramagnetic component (TIP) to the data ($\sim 10^{-3}$ cm^3 mol^{-1}). The magnetization curves of **1** and **4** at 2 K almost saturate at high fields with values of the saturation magnetization M_S of 4.99 $N_A\mu_B$ (**1**) and 4.61 $N_A\mu_B$ (**4**) close to the theoretical value of 5 $N_A\mu_B$ (Figures S7 and S10, SI). The superposition of M versus H/T plots on a single master curve further supports the presence of negligible anisotropy in **1**. In line with this, almost ideal Curie magnetic behavior fits performed with the program PHI[55] (eq S1, SI) reveal for **1** and **4** only very small axial and transversal anisotropy parameters D and E and g values close to the theoretical value of 2.0023193048(8) (Table 2).

In contrast, for the Fe^{2+} complex **2** and even more pronounced for **3**, the dc magnetic curves (χT and magnetization) indicate additional contributions arising from an orbital momentum $L \neq 0$ and influences of anisotropy (Figures 5 and 6 and Figures S8 and S9, SI). Values of χT at 300 K amount to 4.316 cm^3 mol^{-1} K in **2** and 3.780 cm^3 mol^{-1} K in **3**, both being much larger than the theoretical spin-only values of the susceptibilities which amount to 3 and 1.875 cm^3 mol^{-1} K for a high spin d^6 (S = 4/2) and d^7 (S = 3/2) ion, respectively.

Upon a decrease of the temperature, the χT curves of **2** (below 50 K) and **3** (below 150 K) both display a distinct downturn, which is, in the absence of any close M−M contacts, indicative of the presence of zero-field splitting (ZFS) of the spin states in these complexes.[56] In line with these observations, **2** and **3** display values of the molar magnetization M_H at 2 K and 7 T (**2**, 2.79; **3**, 2.45 $N_A\mu_B$), which are below the theoretical values of M_S (S = 4/2) = 4 $N_A\mu_B$ and M_S (S = 3/2) = 3 $N_A\mu_B$ (Figures S8 and S9, SI). Distinctly larger g values for the cobalt complexes **3** and **6** in comparison to those of the iron complexes **2** and **5** can be rationalized by two facts. The idealized d orbital splitting diagram for a trigonal planar complex of D_3 symmetry indicates the probability of a first order orbital contribution to the magnetic moment for a d^7 electron configuration already for the ground state through spin orbit coupling of the electrons in the d_{xz} and d_{yz} orbitals (Figure 7).[57]

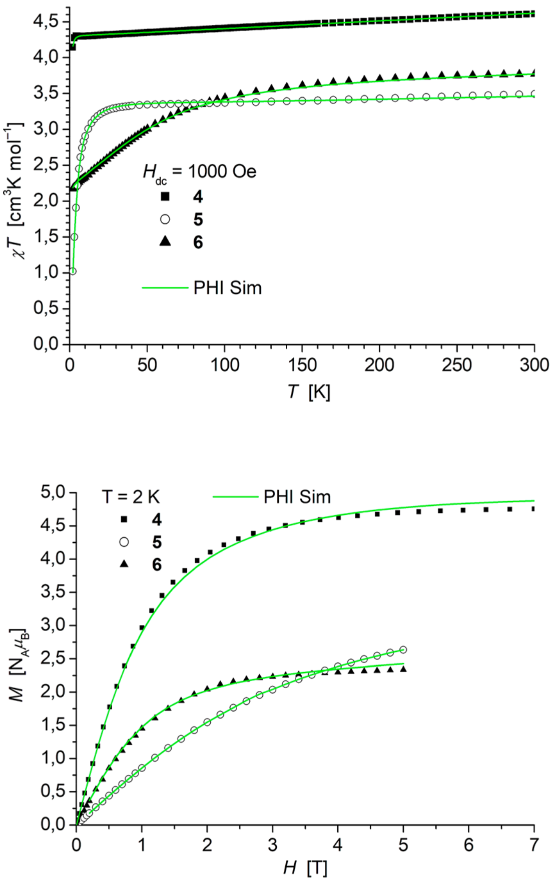

Figure 6. (a) Temperature dependence of χT and (b) plots of magnetization M versus field H at 2 K for **4**−**6**. Solid green lines represent the results of the simultaneous fittings with the temperature dependent magnetization (Table 2 and Figure S11, SI) according to a spin Hamiltonian (eq S1, SI) by the PHI program. Data of **5** and **6** taken from ref 21.

For the iron complexes **2** and **5**, similar contributions can result only from coupling with orbital momenta of excited states. This assumption is supported by distinct values of the temperature independent paramagnetism (TIP) in these complexes (Table 2). In addition, the spin−orbit coupling constants of the free ions are found to be larger for Co^{2+} (-177 cm^{-1}) than for Fe^{2+} (-102 cm^{-1}).[58] Therefore, we also analyzed the dc magnetic data of **3** and **6** for the case of strong orbital interactions (L > 0) with the PHI program by considering an additional spin orbit term ($H_{SO} = \lambda \vec{S} \cdot \vec{L}$) in eq S1, SI. However, these fittings did not result in a proper description of the χT vs T and magnetization curves.

Simultaneous fits of the temperature dependent susceptibility data and the magnetization curves of the iron and cobalt

Table 2. SH Parameters of 1−4 Extracted from a Simultaneous PHI Simulation of the dc Magnetic Data (eq S1, SI and Figures 5 and 6 and Figures S7−S10, SI) Including the Values of 5 and 6 from the Literature[21]

	1	**2**		**3**	
		D pos.	D neg.	D pos.	D neg.
D [cm^{-1}]	0.23(1)	+13.84(6)	−16.85(10)	+47.97(10)	−59.08(14)
E	0.10(1)	4.98(3)	4.99(2)	22.17(8)	12.33(8)
$\|E/D\|$	0.44	0.36	0.30	0.46	0.21
g_x	2.020(1)	2.288(1)	2.260(1)	2.901(3)	2.886(1)
g_y	2.020(1)	2.367(2)	2.260(1)	2.705(1)	2.907(4)
g_z	2.020(1)	2.260(1)	2.337(2)	2.885(1)	2.618(1)
TIP [cm^3 mol^{-1}]	1.29(1)E−3	1.13(1)E−3	1.25(2)E−3	4.06(1)E−4	6.11(1)E−4
residual	0.000300	0.127652	0.033246	0.001070	0.000212

	4	**5**[a]		**6**[a]	
		D pos.	D neg.	D pos.	D neg.
D [cm^{-1}]	−0.48(1)	+9.50(1)	−5.80(1)	+45.42(18)	−50.58(40)
E	−0.20(1)	±0.10(1)	4.84(1)	17.79(15)	13.64(13)
$\|E/D\|$	0.42	0.01	0.83	0.39	0.27
g_x	1.980(1)	2.224(1)	1.957(1)	2.782(1)	2.783
g_y	1.980(1)	2.141(1)	2.092(1)	2.763(1)	2.777
g_z	1.984(2)	2.099(1)	2.179(1)	2.782(1)	2.668
TIP [cm^3 mol^{-1}]	1.08(1)E−3	0.98(20)E−4	0.73(1)E−3	0.81(1)E−3	1.06×10^{-3}
residual	0.003966	0.001022	0.000004	0.001041	0.001222

[a] Data taken from ref 21 and newly fitted with an anisotropic treatment of g.

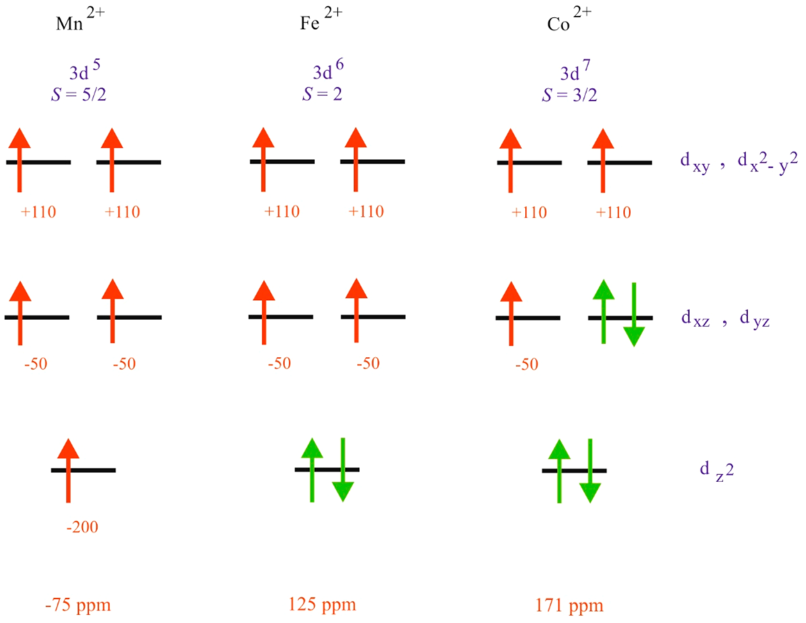

Figure 7. Estimation of paramagnetic ^{7}Li NMR shifts based on idealized electronic configuration schemes[57] of Mn^{2+}, Fe^{2+}, and Co^{2+} in an ideal triangular planar coordination. At the bottom, the observed overall NMR shifts are listed while the small numbers at the energy levels give the estimated contribution of each orbital. Only the unpaired (red) spins contribute to the overall NMR shift.

complexes **2**, **3**, **5**, and **6** performed with the program PHI[55] (eq S1, SI) are distinctly improved by the use/inclusion of the anisotropy parameters D and E as well as an anisotropic treatment of the g parameter (Table 2). In this case, any possible contributions arising from $L \neq 0$ are included in these parameters. Furthermore, we realized that partially multiple solutions of similar fitting quality exist for the same set of data altogether suggesting that the given parameters in Table 2 have to be considered critically. Absolute values and signs of these parameters can reliably only be determined by magnetic measurements on single crystals and/or EPR measurements.[59,60]

A comparison of the magnetic dc curves of the ate complexes **1**−**3** with those of the ion-separated ones of **4**−**6** reveals that the characteristics are in a broader sense not distinctly different. Therefore, one can at least conclude that the distortion of the planar trigonal symmetry around the central metal atoms upon coordination of the lithium atoms has a minor influence on the dc magnetic properties of the compounds.

AC Magnetic Measurements. In addition to the static (dc) magnetic data, also dynamic (ac) magnetic measurements were performed for **1**−**4** (Figures 8 and 9 and Figures S11−S18). Those of **5** and **6** have been already published.[21]

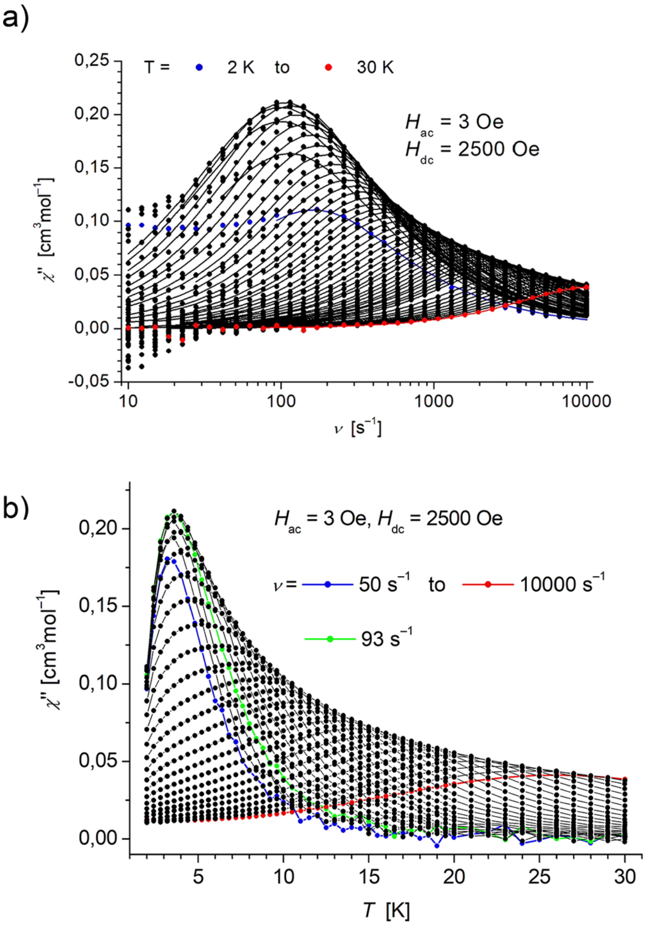

Figure 8. (a) Frequency dependence and (b) temperature dependence of the out of phase χ'' component of the ac magnetic susceptibility of **1** at 2500 Oe at different temperatures (a) and frequencies (b) measured with a PPMS (Quantum Design) Dynacool magnetometer with an oscillating ac field of 3 Oe and ac frequencies ranging from 10 to 10 000 s^{-1}. Solid lines represent the fits according to eqs S2 and S3.

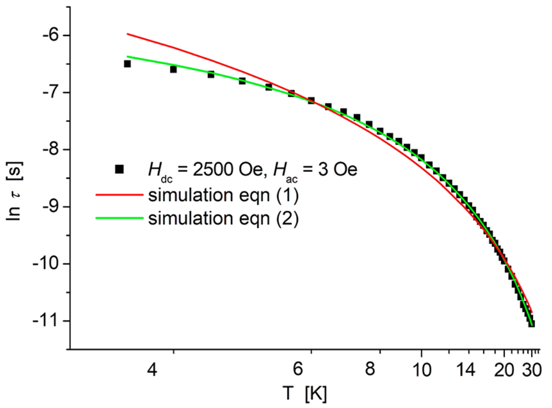

Figure 9. Relaxation time (τ) versus temperature (T) for **1**. Red and green lines represent fits according to eqs 1 and 2, respectively.

Field dependent ac measurements[61] in a range from 0 to 5000 Oe were performed for **1**−**4** at 2 K using a 3.0 Oe ac field, oscillating at an extended range of frequencies between 1 and 1500 s^{-1} (Figures S11−S13, SI). In the absence of an external dc field (H_{dc} = 0), the out-of-phase component of the ac susceptibility (χ'') of all complexes has much lower intensity than the in-phase component (χ') and displays no maximum, indicating that spin−lattice relaxation is faster than the time scale of the experiment. With the application of a static dc field, the intensity of χ'' is significantly enhanced for **1**, **3**, and **4** but not for **2**. The manganese complexes **1** and **4** both show curves with maxima, which are distinctly broad in the case of **4**. In contrast, **3** displays an increase of χ'' both at lower and higher frequencies but with maxima lying outside the frequency window. This is indicative for spin−lattice relaxation processes, which are slightly slower/faster than the time scale of the experiment.

For **1**, an attempt was made to extract magnetic relaxation times measuring the frequency dependencies at different temperatures at a constant dc field of 2500 Oe by fits of the resulting curves to eqs S2 and S3 (Figure 8 and Figures S14 and S15, SI). Measurements were performed for two different frequency ranges of 1−1500 s^{-1} and 10−10 000 s^{-1} on a Magnetic Property Measurement System (MPMS) and a Physical Property Measurement System (PPMS), respectively.

Plots of the relaxation time τ of **1** vs the reciprocal temperature show a curvature feature upon increase of the temperature with a pseudolinear behavior at temperatures above 15 K (Figure 9). However, as already pointed out by others who observed slow magnetic relaxation phenomena in Mn(II) compounds, the almost isotropic magnetic dc behavior of **1** makes an Orbach relaxation mechanism via a magnetic energy barrier rather improbable.[62−64] In some of these papers, the authors found indications for the occurrence of a process governed by a phonon bottleneck effect. A phonon bottleneck occurs in a one-phonon direct relaxation process when the emitted phonons have nowhere to go because of inefficient energy transfer of the lattice to the environment, so the emitted phonon can be reabsorbed, affecting the spin relaxation.[65] Therefore, and in analogy to the paper of da Cunha et al.,[66] the whole temperature dependence of τ was first fitted by a simple power law, eq 1.

$$\tau^{-1} = AT^{n} \tag{1}$$

A rough agreement with the curve of the experimental data of τ can be obtained with parameter A = 20.69 $\text{s}^{-1}\ \text{K}^{-n}$ and an exponent n = 2.3 (red line in Figure 9), the latter number being close to 2, which is thought to be characteristic for a phonon bottleneck determined relaxation behavior.[65] A slightly better agreement can be obtained by the use of eq 2 as the fit function including a direct (T^{1}) and a Raman (T^{3}) process (green line in Figure 9) with parameters A_{Dir} = 174.7 s^{-1} K and B_{Ram} = 2.03 $\text{s}^{-1}\ \text{K}^{-3}$.[67]

$$\tau^{-1} = A_{\text{Dir}}T + B_{\text{Ram}}T^{3} \tag{2}$$

The Cole−Cole/Argand plots of χ'' vs χ' (see Figure S16, SI) show semicircular isotherms. Values of the coefficient α, that defines the distribution of relaxation times within the generalized Debye model, were found to increase below 15 K, which supports the presence of multiple relaxation processes at lower temperatures (Figure S17, SI). The temperature dependence of χ'' reveals a distinct broadening of the maximum above 98 s^{-1} (Figure 8).

We note that the low temperature data of **1** measured on the PPMS displayed below 3.2 K an unusual decrease of τ with a decrease of the temperature, which was not found for a sample measured at an MPMS (Figure S18, SI).

^{7}Li NMR Spectroscopy. Figure 10 shows the ^{7}Li MAS NMR spectra of **1**−**3** (for full range ^{7}Li MAS NMR spectra

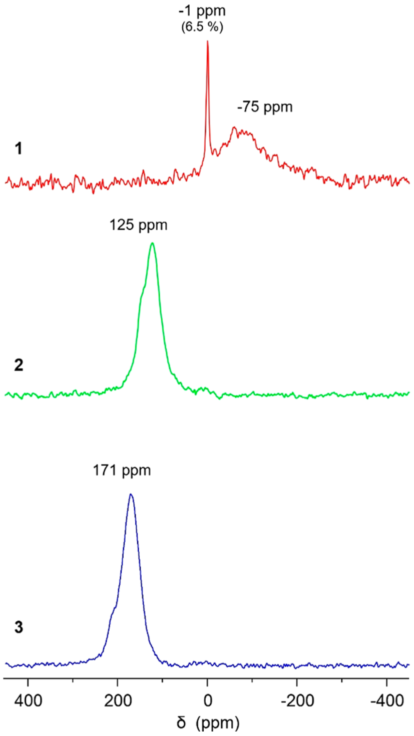

Figure 10. ^{7}Li MAS NMR spectra of **1**−**3**.

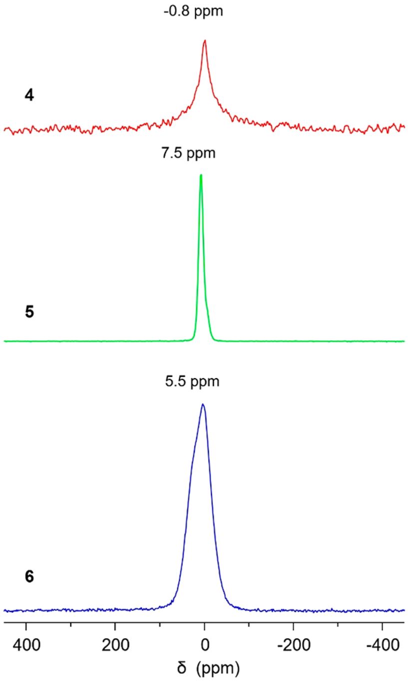

Figure 11. ^{7}Li MAS NMR spectra of **4**−**6**.

including spinning sidebands, see Figure S19, SI). In these compounds, the transition metal is located in a nitrogen triangle with Li located just next to this triangle, i.e., connected to the transition metal via two μ_2-N bonds. While **2** and **3** show broad peaks with large positive shifts of 125 and 171 ppm, respectively, compound **1** displays a very broad peak with a large negative shift of −75 ppm. For **1**−**3**, an additional small peak is detected around −1 ppm, which might result from excess $LiN(SiMe_3)_2$ or slight decomposition during the measurement. The large positive and negative shift values of the main peaks clearly show that unpaired electron spin density is transferred from the divalent transition metal ions to the lithium nuclei, while the different signs hint at different contributions from the different 3d orbitals.

In contrast to that, **4**−**6** show peaks with much smaller shifts of 7.5 ppm, 5.5 ppm, and −0.8 ppm, respectively, which agree well with the much larger distance between Li and the transition metal ions in these compounds (Figure 11 and Figure S19, SI). As expected, pure lithium(bistrimethylsilyl)-amide shows a narrow line with a very small shift of 1 ppm (Figure S20, SI).

A simple correlation of the absolute magnetic moment of **1**−**3** at room temperature with the observed paramagnetic shifts in the ^{7}Li NMR spectra in the sense that a higher μ_{eff} at room temperature results in a stronger absolute shift seems to be not meaningful. We therefore propose, in accordance with examples from the literature,[39,42] a simple attempt to rationalize the observed NMR shifts as depicted in Figure 7. In a triangular planar coordination with nitrogen, the energy levels of the 3d orbitals of the transition metals should be unequal. The d_{z^2} orbital, being aligned perpendicular to the N triangle, should have the lowest energy. The d_{xy} and $d_{x^2-y^2}$ orbitals, being aligned within the plane of the N triangle, have the highest energy, and the energy of the d_{xz} and d_{yz} orbitals should have an intermediate position. Due to the symmetry of these orbitals, we expect equal contributions to the overall observed NMR shift for d_{xy}, $d_{x^2-y^2}$, and for d_{xz}, d_{yz}.

The electron configurations of the divalent transition metals are Mn^{2+}, $3d^5$; Fe^{2+}, $3d^6$; and Co^{2+}, $3d^7$. Therefore, in a high-spin configuration, the number of unpaired electron spins contributing to the overall NMR shift is 5, 4, and 3 for Mn^{2+}, Fe^{2+}, and Co^{2+}, respectively. When comparing the situation for Fe^{2+} and Co^{2+}, we see that the difference in NMR shifts (about −50 ppm) is caused by one unpaired electron in the d_{xz} orbital (or d_{yz}), and we can thus assign this value to the contribution of this orbital. With this value, the contribution of the d_{xy} and $d_{x^2-y^2}$ orbitals can be estimated from the observed NMR shifts to be about +110 ppm (Fe^{2+}: (125 ppm + 2 × 50 ppm)/2 = 112.5 ppm; Co^{2+}: (171 ppm + 50 ppm)/2 = 110.5 ppm). Finally, these values can be used to estimate the contribution of the d_{z^2} orbital to the NMR shift of Mn^{2+} to be −75 ppm + 2 × 50 ppm to −2 × 110 ppm ≈ −200 ppm.

A more stringent calculation of the different contributions would be solving the equations

$$2\alpha + 2\beta + \gamma = -75\ \text{ppm} \tag{3}$$

$$2\alpha + 2\beta = 125\ \text{ppm} \tag{4}$$

$$2\alpha + \beta = 171\ \text{ppm} \tag{5}$$

where α, β, and γ are the contributions from the different orbitals, and the solution would be α = 108.5 ppm, β = −46 ppm, and γ = −200 ppm.

In addition to the NMR spectra in the solid state, measurements were also performed on solutions (**1**−**3**, C_6D_6; **4**−**6**, thf-d_8). The ^{7}Li NMR spectra display for **1** a large negative shift of −88 ppm, whereas **2** and **3** show large positive shifts of 153 and 213 ppm, respectively (Figure 12). The same trend has been observed for the solid samples (Figure 10), although the absolute values for the shifts are consistently larger for the liquid samples by about 25%. This could be caused by different effective temperatures of the liquid and solid samples. While all measurements have been

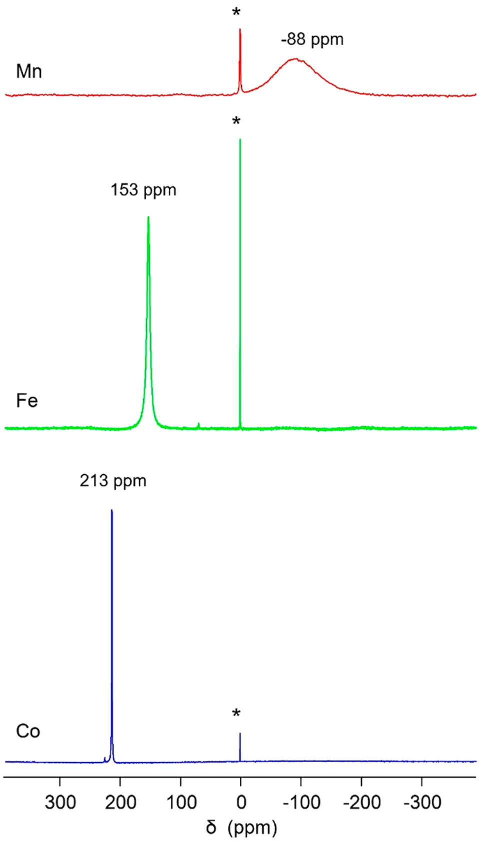

Figure 12. ^{7}Li NMR spectra of **1**−**3** dissolved in C_6D_6. Minor diamagnetic impurities are marked with an asterisk and could originate from slight amounts of unreacted $LiN(SiMe_3)_2$ or indicate partial dissociation in solution.

performed nominally at room temperature, the fast magic-angle spinning used for the solid samples is associated with some air friction and thus leads to an increase of the sample temperature and, thus, according to Curie's law, to a reduction of the paramagnetic shifts.

In addition to the paramagnetic shifts, the solution spectra also reflect the observed differences in the peak widths of the ^{7}Li solid-state spectra of **1**−**3** (Table 3). Although measured by MAS, NMR signals of solid-state samples are in general found to be broader than their analog in solution, which is also observed for **1**−**3**. In addition, the ^{7}Li signal of the manganese complex **1** is found to be much broader than those of **2** and **3**, both in the solid state and in solution. For the ^{7}Li spectra in solution, there is also a distinct difference in the peak width between the signal of **2** and **3** with the latter being much smaller. This trend of different peak broadening by paramagnetic metal ions is in general reflected also by the solution ^{1}H NMR spectra of **1**−**6** (not shown), which display only slightly broadened peaks for **3** and **6** (fwhm: 50−200 Hz), a medium broadening in **2** and **5** (fwhm: 480−620 Hz), and nearly featureless very broad peaks of **1** and **4** (fwhm: ∼13 000−19 000 Hz).

Table 3. ^{7}Li NMR Peak Shifts [ppm] and Widths [Hz] of 1−3 in Solid State and Dissolved in C_6D_6 (Figures 10 and 12)

	1		**2**		**3**	
	shift	width	shift	width	shift	width
solid[a]	−74.6	11200	122.0	3100	168.0	3490
liquid	−92.1	16800	152.9	1110	213.4	93

[a] MAS NMR; values given for isotropic peaks.

These observations can be rationalized as follows. In samples with paramagnetic ions, the magnetic moment of the electron spin has also a distinct influence on the relaxation behavior of the nuclear spin and thus on the line width of NMR signals. In general, the observability of sharp NMR signals requires long nuclear relaxation times. Davis et al. have pointed out and confirmed in a recent paper that the transverse relaxation time of the nucleus T_{2N} has an inverse dependence on the electron relaxation time T_{1e}.[68] This oppositional behavior is discussed and explained in more detail, for example, in a paper by Satterlee.[69] Briefly concluded, this leads to the fact that metal ions with the tendency to exhibit smaller magnetic anisotropies in general (independently of the specific coordination) like Cu^{2+} and Mn^{2+} give rise to lower electron relaxation rates ($T_{1e}^{-1} \sim 10^8$ to 10^9 s^{-1}) and result in broad NMR signals, whereas ions which comprise orbitally degenerate ground states and/or low lying excited states like Co^{2+} or Fe^{2+} and possess faster electron relaxation rates ($T_{1e}^{-1} > 10^{10}$ s^{-1}) and therefore enable the observation of sharper NMR signals. This exactly reflects the observations made in the dc magnetic measurements on solid samples **1**−**6** with respect to the influences of magnetic anisotropy in the different metal complexes.

Therefore, the results of ^{7}Li and ^{1}H NMR in solution give strong evidence that the local structure around the transition metal ions including the neighboring Li ions is preserved.

Quantum Chemical Calculations. Mondal and Kaupp calculated NMR shifts for $LiMPO_4$ (M = Mn, Fe, Co, Ni) with a combination of periodic and cluster models, taking into account zero-field splitting and pseudocontact.[48] Orbital shielding and hyperfine couplings were calculated by them with hybrid density functionals and supercell models, whereas *g* tensors and zero-field-splitting tensors were obtained from cluster models and CASSCF. In that study, a pronounced effect of the exchange fraction on the hyperfine coupling was found. Nowotny et al. employed embedded cluster models and the PBE0 hybrid functional to calculate NMR shifts of Cr(III) and Cu(II) compounds.[70] Spin−orbit effects were taken into account with the ZORA approach. Ott et al. calculated the diamagnetic orbital shift, the Fermi-contact shift, and the pseudocontact shift of iron(II) hydrido complexes in solution with B3LYP.[71] They found that inclusion of the pseudocontact shift led to a significantly better agreement with the experiment. A simple point−dipole approximation deviates from an exact integration by 10−20% for atoms with small distances to the transition metal. Analytical expressions for the pseudocontact shift are given by Suturina and co-workers.[72]

All of these authors agree that the NMR shift in paramagnetic compounds is the sum of three contributions, the diamagnetic orbital shift δ_{dos}, the Fermi-contact shift δ_{fcs}, and the pseudocontact shift δ_{pcs}.[73]

$$\delta_{theo} = \delta_{dos} + \delta_{fcs} + \delta_{pcs}$$

In this study, δ_{dos} is calculated with the NMR shielding option of VASP on the basis of PBE+U wave functions.[74] δ_{fcs} is estimated from the isotropic hyperfine coupling constants (hfcc) calculated with hybrid DFT applying CRYSTAL17 (version 1.0.1; eq S4, SI),[75] and δ_{pcs} is approximated by the point-dipole approximation from the magnetic susceptibility tensors χ obtained with VASP (eq S5, SI). Since the axial

Table 4. Calculated ^{7}Li NMR Peak Shifts δ_{theo} [ppm] in Compounds 1−3 with Respect to LiCl and Their Contributions δ_{dos}, δ_{fcs}, and δ_{pcs} [ppm]

			δ_{fcs}[a]			δ_{theo}		
compound	δ_{dos}	δ_{pcs}	B3LYP	M06	PWxPW	B3LYP	M06	PWxPW
1	+33.9	−3.9	−306.1	−168.9	−215.4	−276.1	−138.9	−185.4
2	+32.8	+31.3	−77.8	−3.0	−6.7	−13.7	+61.1	+57.4
3	+33.2	+1.8	+66.2	+36.6	+110.5	+101.2	+71.6	+145.5

[a] δ_{fcs} was calculated with the hybrid functionals B3LYP, M06, and PWxPW.

anisotropy $\chi_{zz} - (\chi_{xx} + \chi_{yy})/2$[76] is relatively small for all compounds, due to the local symmetry of the transition metals, we accept the anticipated error of 10−20%. As it was found previously,[48] that the hfcc's are strongly method dependent, we selected three different hybrid functionals, B3LYP,[77] M06,[78] and PW1PW,[79] with a reduced amount of Fock exchange[80] for comparison (PWxPW). δ_{fcs} was estimated from the hfcc using the approach of Grey et al.[44,46] The theoretical results are summarized in Table 4. The reference compound for the NMR shifts was in all cases bulk LiCl.

The diamagnetic orbital shift is quite similar for the three compounds, ∼33 ppm. Due to the small anisotropy, the pseudocontact shift is small, except for the Fe compound (+31 ppm). As found in previous theoretical studies, the Fermi-contact shift (respectively, the small spin density at the Li position) is very sensitive to the choice of the density functional, and also to numerical details of the calculations. All three functionals agree about the trend, with a strong negative shift for **1**, an intermediate shift for **2**, and a large positive shift for **3**. However, the absolute agreement with the experimentally observed NMR shifts, −75 ppm (**1**), +125 ppm (**2**), and +171 ppm (**3**), is not satisfactory for all three methods. The largest mean deviation is obtained with the popular B3LYP functional that has been successfully applied in earlier studies.[44,46] M06 does not reproduce the large difference between compounds **2** and **3**. Overall, the PWxPW functional follows most closely the experimental shifts.

■ CONCLUSION

The ate complexes [LiM{N(SiMe$_3$)$_2$}$_3$] (M^{2+} = Mn, Fe, Co) with the lithium atoms connected to the 3d metal atoms manganese, iron, or cobalt via μ_2 nitrogen bridges were found to display strong ^{7}Li NMR paramagnetic shifts of about −75, 125, and 171 ppm, respectively, whereas shifts for the lithium ions in [Li(15-crown-5)][M{N(SiMe$_3$)$_2$}$_3$], coordinated by the 15- crown-5 ether, are close to zero.

The comparison with the results from the dc magnetic measurements suggests that there exists no simple correlation of absolute magnetic moment of the ate complexes at room temperature with the observed paramagnetic shifts in the ^{7}Li NMR spectra in the sense that a higher μ_{eff} at room temperature results in a stronger absolute shift. On the other hand, the different magnitudes of the observed NMR peak widths for the different metal ion complexes roughly correlates with the amount of magnetic anisotropy derived from the dc magnetic data. For the paramagnetic shifts, a simple model was proposed in accordance with examples from the literature, which accounts for different d-orbital contributions based on the splitting diagram for a trigonal planar coordination. In addition, an attempt was made to calculate the paramagnetic shifts with a combination of GGA+U and hybrid density functional theory. It was found that the calculations of the Fermi-contact shift are very sensitive to numerical aspects of the calculations and the choice of the method, due to the extremely small spin density at the positions of the lithium nuclei. A semiquantitative agreement between experiment and theory could be obtained with triple-ζ basis sets and a modified version of the PW1PW functional. Here, it is strongly desirable to improve the numerical stability of the calculations. Nonetheless, the present results should be useful for future predictions of paramagnetic NMR shifts mediated via nitrogen bonds.

Field- and temperature-dependent ac magnetic measurements reveal slow magnetic relaxation processes for [LiMn{N(SiMe$_3$)$_2$}$_3$] at low temperatures. As magnetic dc curves suggest an almost isotropic behavior, this observation could be related to a phonon bottleneck effect.

■ EXPERIMENTAL SECTION

Synthesis. Standard Schlenk techniques were employed throughout the syntheses using a double manifold vacuum line with high purity dry nitrogen (99.9994%) and an MBraun glovebox with high purity dry argon (99.9990%). The solvents heptane and pentane were dried over LiAlH$_4$, and the solvent toluene was dried over sodium-benzophenone. All were distilled under nitrogen. LiN(SiMe$_3$)$_2$ and 15-Crown-5 were purchased from Sigma-Aldrich. LiN(SiMe$_3$)$_2$ was distilled in a vacuum prior to use (bp 80−84 °C/0.01 Torr). [M{N(SiMe$_3$)$_2$}$_2$]$_2$ (M = Mn,[81] Co[82]), [LiFe{N(SiMe$_3$)$_2$}$_3$] (**2**), [Li(15-crown-5)][Fe{N(SiMe$_3$)$_2$}$_3$] (**5**), and [Li(15-crown-5)][Co{N(SiMe$_3$)$_2$}$_3$] (**6**)[21] were prepared according to literature procedures.

[LiMn{N(SiMe$_3$)$_2$}$_3$] **(1)**. [Mn{N(SiMe$_3$)$_2$}$_2$]$_2$ (0.500 g, 0.665 mmol) and Li N(SiMe$_3$)$_2$ (0.223 g, 1.33 mmol) were dissolved in 3 mL of heptane at room temperature to give a pale pink solution. After 2 h of reaction time, the solution was stored for 4 h in the fridge and then moved to a freezer to yield after 2 days pale pink crystalline clumps of **3**. The supernatant solution was decanted off at −75 °C and the crystals washed two times with pentane at this temperature to yield 510 mg (71%) of **3** after drying in a vacuum.

$C_{18}H_{54}MnLiN_3Si_6$ (543.03) calcd.: C, 39.81; H, 10.02; N, 7.74. Found: C, 39.33; H, 9.86; N, 7.83%.

^{1}H NMR (500 MHz, C_6D_6, 295 K): Besides the solvent and impurity (HN(SiMe$_3$)$_2$ and LiN(SiMe$_3$)$_2$) peaks, one very broad asymmetric peak around 32 ppm in a range from −400 to 400 ppm was found (−SiMe$_3$ terminal and bridging, 36H).

[LiFe{N(SiMe$_3$)$_2$}$_3$] **(2)**. [LiFe{N(SiMe$_3$)$_2$}$_3$] was prepared according to ref 37. ^{1}H NMR (500 MHz, C_6D_6, 295 K): 9.02 ppm (br (∼623 Hz) s, −SiMe$_3$ (terminal), 9H), −3.12 ppm (br (∼478 Hz) s, −SiMe$_3$ (bridging), 18H). Quantitative integration was, due to signal broadness and overlapping with solvent peaks, not exactly possible; approximate ratio, 0.4:1.

[LiCo{N(SiMe$_3$)$_2$}$_3$] **(3)**. [Co{N(SiMe$_3$)$_2$}$_2$]$_2$ (0.250 g, 0.329 mmol) and Li N(SiMe$_3$)$_2$ (0.110 g, 0.658 mmol) were dissolved in 4 mL of heptane. Upon stirring at room temperature, the color of the solution gradually changed from dark green to light green. After 2 h of reaction time, the solution was stored for 4 h in the fridge and then moved to a freezer to yield after one night light green crystals of **3**. The supernatant solution was decanted off at −75 °C and the crystals

washed two times with pentane at this temperature to yield 310 mg (86%) of **3** after drying in a vacuum.

$C_{18}H_{54}CoLiN_3Si_6$ (547.03) calcd.: C, 39.52; H, 9.95; N, 7.68. Found: C, 39.06; H, 9.81; N, 7.95%.

^{1}H NMR (500 MHz, C_6D_6, 295 K): 14.14 ppm (br (∼205 Hz) s, −SiMe$_3$ (terminal). 0.5, 9H), −12.41 ppm (br (∼134 Hz) s, −SiMe$_3$ (bridging), 1, 18H).

*[Li(15-crown-5)][Mn{N(SiMe$_3$)$_2$}$_3$] (**4**).* [Mn{N(SiMe$_3$)$_2$}$_2$]$_2$ (0.250 g, 0.332 mmol) and Li N(SiMe$_3$)$_2$ (0.111 g, 0.666 mmol) were dissolved in 4 mL of toluene. The addition of 15-crown-5 (0.13 mL, 0.666 mmol) resulted in the formation of a heavier light pink and a lighter slightly yellowish phase. Upon storage in a freezer (−43 °C), the solution almost completely solidified in between 1 h and turned to a pale pink crystalline clump and a colorless solution when stored for one night in a fridge. The supernatant solution was decanted off, and the crystalline material was washed two times with a mixture of toluene/pentane 1:2 at −20 °C and finally dried in a vacuum at room temperature to give 480 mg of **4** (85%)

$C_{28}H_{74}LiMnN_3O_5Si_6$ (763.30 g/mol) calcd.: C, 44.06; H, 9.77; N, 5.51. Found: C, 43.60; H, 9.37; N, 5.89%.

^{1}H NMR (500 MHz, thf-d$_8$, 295 K): 31 ppm (br (∼12 400 Hz), s, −SiMe$_3$, 36H), 3.70 ppm (br, s, −15K5, 20H). Quantitative integration was, due to extreme signal broadness (protons of the −SiMe$_3$ groups) and partial overlapping with thf solvent peaks (protons of 15K5), not possible.

*[Li(15-crown-5)][Fe{N(SiMe$_3$)$_2$}$_3$] (**5**).* [Li(15-crown-5)][Fe{N(SiMe$_3$)$_2$}$_3$] was prepared according to ref 21. ^{1}H NMR (300 MHz, thf-d$_8$, 295 K): 3.35 ppm (br (∼16 Hz) s, −15K5, 20H), −2.38 ppm (br (∼549 Hz) s, −SiMe$_3$, 36H). Quantitative integration was, due to signal broadness and partial overlapping with solvent peaks, not exactly possible; approximate ratio, 0.66:1.

[Li(15-crown-5)][Co{N(SiMe$_3$)$_2$}$_3$] (**6**): [Li(15-crown-5)][Co{N(SiMe$_3$)$_2$}$_3$] was prepared according to ref 21. ^{1}H NMR (300 MHz, thf-d$_8$, 295 K): 2.61 ppm (s (∼4 Hz), −15K5, 0.42, 20H), −7.74 ppm (br (∼50 Hz) s, −SiMe$_3$, 1, 36H).

Crystallography. Due to the air and moisture sensitivity of the compounds, crystals suitable for single crystal X-ray diffraction were selected in perfluoroalkylether oil in an Ar filled glovebox and mounted quickly to the diffractometer equipped with an Oxford Cryosystem.

Single-crystal X-ray diffraction data of **1** and **4** were collected using Ga Kα radiation (λ = 1.34143 Å) generated by a Ga Metaljet D2 with a multilayer optic on a STOE STADI Vari (Dectris Eiger Hybrid Pixel Detector 4M).

Single-crystal X-ray diffraction data of **3** were collected using Mo Kα radiation (λ = 0.71073 Å) generated by a microfocus sealed X-ray tube (Mo Genix 3D) with a multilayer optic on a STOE STADI Vari (Pilatus Hybrid Pixel Detector 300 K).

Raw intensity data were collected and treated with the STOE X-Area software, version 1.82. Data for all compounds were corrected for Lorentz and polarization effects. With the implemented program STOE LANA, Interframe scaling of the data sets was done as well as Multiscan absorption corrections applied by scaling of reflection intensities.[83]

Using Olex2,[84] the structures were solved with the ShelXT[85] structure solution program using intrinsic phasing and refined with using least squares minimization.

Molecular diagrams were prepared using Diamond.[86]

In **1**, **3**, and **4**, all Mn, Co, Li, O, N, and C atoms were refined with anisotropic displacement parameters, while H atoms were computed and refined using a riding model, with the isotropic temperature factor equal to 1.2 times the equivalent temperature factor of the atom to which they are linked. In **3**, the C atoms of two methyl groups were refined with a split model of site disorder. A disordered toluene solvent molecule was identified and refined with a split model of site disorder in **4**.

CCDC-2109946 (**1**), 2109945 (**3**), and 2109944 (**4**) contain the supplementary crystallographic data for this paper. These data can be obtained free of charge at www.ccdc.cam.ac.uk/conts/retrieving.html (or from the Cambridge Crystallographic Data Centre, 12 Union Road, Cambridge CB2 1EZ, UK; fax: (internat.) + 44−1223/336-033; E-mail: deposit@ccdc.cam.ac.uk).

X-ray powder diffraction patterns (PXRD) for **1**−**6** (powder of crystals) were measured at room temperature on a STOE STADI P diffractometer (Cu K$_{\alpha 1}$ radiation, germanium monochromator, Debye−Scherrer geometry, Mythen 1K detector) in sealed glass capillaries. The theoretical powder diffraction patterns were calculated based on the atom coordinates obtained from single crystal X-ray analysis (180 K) by using the program package STOE WinXPOW.[87]

Physical Measurements. ^{1}H and ^{7}Li NMR spectroscopy in solution were performed on a Bruker Avance 300 MHz or a Bruker AvanceIII 500 MHz spectrometer at 295 K.

^{7}Li magic-angle spinning nuclear (MAS) NMR spectroscopy was performed at a magnetic field of 4.7 T corresponding to a ^{7}Li resonance frequency of 77.8 MHz. Sample spinning was done with 1.3 mm rotors at 60 kHz. Spectra were acquired with a Hahn-echo pulse sequence with a $\pi/2$ pulse length of 0.65 μs and a recycle delay between 1 and 10 s.

C, H, and N elemental analyses were performed on an Elementar Vario Micro Cube instrument.

Solid-state UV−vis absorption spectra of **1** and **4** were measured on a PerkinElmer Lambda 900 spectrophotometer equipped with a Labsphere integrating sphere in reflection mode for samples which were prepared as micron-sized crystalline powders in quartz cuvettes.

Solution UV−vis absorption spectra of **1**−**3** (C_6D_6) and **4** (thf) were measured on the same instrument in absorption mode in quartz cuvettes.

Zero-field-cooled temperature dependent susceptibilities were recorded in dc mode using a MPMS-III or MPMS-XL (Quantum Design) SQUID magnetometer over a temperature range from 2 to 300 K in a homogeneous 0.1 T external magnetic field. The magnetization curves were measured on the same instrument up to a dc field of 7 T. The ac susceptibility measurements have been performed using a MPMS-XL (Quantum Design) SQUID magnetometer with an oscillating ac field of 3 Oe and ac frequencies ranging from 1 to 1500 Hz or a PPMS (Quantum Design) Dynacool magnetometer with an oscillating ac field of 3 Oe and ac frequencies ranging from 10 to 10 000 Hz. The samples were contained in gelatin capsules filled in a glovebox under an argon atmosphere owing to the high degree of moisture and oxygen sensitivity of the compounds. The samples were transferred in sealed Schlenk tubes from the glovebox to the magnetometer and then rapidly transferred to the helium-purged sample space of the magnetometer. The data were corrected for the sample holder including the gelatin capsule and for diamagnetism using Pascal's constants.[60,88,89]

Details about the simulations are given in the Supporting Information.

Quantum Chemical Calculations. Hyperfine couplings were computed with the crystal orbital program package CRYSTAL17 version 1.0.2 (eq S4, SI).[75] All-electron basis sets of triple-ζ valence with polarization quality optimized for solid-state calculations were used for all atoms.[90] Full structure optimizations of lattice parameters and atom positions were performed with the hybrid functional PW1PW[79] with 25% Fock exchange contribution. In these calculations, increased integral accuracy tolerances TOLINTEG 7,7,7,14,42 and moderate Monkhorst−Pack shrinking factors 4 × 2 × 2 were employed. In the hyperfine coupling constant calculations, the density of the Monkhorst−Pack grids was increased to 8 × 8 × 4 (**1**) and 8 × 4 × 4 (**2**, **3**), respectively. A modification of PW1PW denoted as PWxPW[80] with 15% Fock exchange contribution was used here, as well as the hybrid functionals B3LYP[77] (20%) and M06[78] (27%). The hyperfine coupling constants were calculated with version 1.0.1 due to a bug in the newer version 1.0.2, which was used for the optimizations. The calculations were performed for ferromagnetic states where all transition metals were initially assigned a high-spin state. The resulting atomic spin densities in units of μ_B were 4.77 (**1**), 3.71 (**2**), and 2.62 (**3**). In the Experimental Section, a low-spin state was suggested for Co. Attempts to calculate a wave function for this state were not successful due to convergence issues in the self-consistent field procedure. The discrepancies between the calculated and measured NMR shifts are possibly due to the restriction to one magnetic state.

The diamagnetic orbital shift and the magnetic susceptibility tensor were calculated with the plane-wave program VASP version 6.1.2 (eq S5, SI).[91] A cutoff energy of 900 eV was used to describe the crystal orbitals. Core orbitals were represented by the projector augmented wave method.[92] The following POTCAR files were used: Mn_sv_GW, Fe_sv_GW, Co_sv_GW, Si_sv_GW, N_GW_new, C_GW_new, H_GW, and Li_AE_GW. Since hybrid functionals are computationally too demanding with VASP, we used the PBE functional[74] and the simplified GGA+U approach[93] with U = 5 eV on the transition metal atoms. A unified *k* spacing of 0.5 $Å^{-1}$ was employed for the Monkhorst–Pack grid.

■ ASSOCIATED CONTENT

● Supporting Information

The Supporting Information is available free of charge at https://pubs.acs.org/doi/10.1021/acs.inorgchem.1c03237.

> Equations for magnetic simulations and quantum chemical calculations, crystallographic data, molecular structures, XRD powder patterns, magnetic data (PDF)

Accession Codes

CCDC 2109944–2109946 contain the supplementary crystallographic data for this paper. These data can be obtained free of charge via www.ccdc.cam.ac.uk/data_request/cif, or by emailing data_request@ccdc.cam.ac.uk, or by contacting The Cambridge Crystallographic Data Centre, 12 Union Road, Cambridge CB2 1EZ, UK; fax: +44 1223 336033.

■ AUTHOR INFORMATION

Corresponding Author

Andreas Eichhöfer − *Institute of Nanotechnology, Karlsruhe Institute of Technology (KIT), Campus Nord, 76344 Eggenstein-Leopoldshafen, Germany; Karlsruhe Nano Micro Facility (KNMF), 76344 Eggenstein-Leopoldshafen, Germany;* orcid.org/0000-0002-3412-6280; Phone: 49-(0)721-608-26371; Email: andreas.eichhoefer@kit.edu; Fax: 49-(0)721-608-26368

Authors

Sylvio Indris − *Institute for Applied Materials - Energy Storage Systems (IAM-ESS), Karlsruhe Institute of Technology (KIT), 76344 Eggenstein-Leopoldshafen, Germany;* orcid.org/0000-0002-5100-113X

Thomas Bredow − *Mulliken Center for Theoretical Chemistry, Institut für Physikalische und Theoretische Chemie, Universität Bonn, 53115 Bonn, Germany*

Björn Schwarz − *Institute for Applied Materials - Energy Storage Systems (IAM-ESS), Karlsruhe Institute of Technology (KIT), 76344 Eggenstein-Leopoldshafen, Germany;* orcid.org/0000-0002-9461-1448

Complete contact information is available at: https://pubs.acs.org/10.1021/acs.inorgchem.1c03237

Author Contributions

S.I., Li MAS NMR; T.B., quantum chemical calculations; B.S., magnetic AC measurements; A.E., synthesis and characterization

Notes

The authors declare no competing financial interest.

■ ACKNOWLEDGMENTS

This work was supported by the Karlsruher Institut für Technologie (KIT, Campus Nord) and the Karlsruhe Nano-Micro-Facility (KNMF). A.E. thanks A. K. Powell for generous support. T.B. thanks the Paderborn Center for Parallel Computing (pc2) and Leibniz Universität IT Services (LUIS) for providing computational resources.

■ REFERENCES

(1) Power, P. P. Stable two-coordinate, open-shell (d^1–d^9) transition metal complexes. *Chem. Rev.* **2012**, *112*, 3482–3507.

(2) Power, P. P. Two-Coordination in Open Shell (d^0–d^9) Molecular Transition Metal Species: Recent Developments. *Chemtracts* **1994**, *6*, 181–194.

(3) Lappert, M. F.; Power, P. P.; Sanger, A. R.; Srivastava, R. C. In *Metal and Metalloid Amides*; Ellis Horwood, Ltd.: Chichester, 1980.

(4) Nguyen, T.; Panda, A.; Olmstead, M. M.; Richards, A. F.; Stender, M.; Brynda, M.; Power, P. P. Synthesis and characterization of quasi-two-coordinate transition metal dithiolates $M(SAr^*)_2$ (M = Cr, Mn, Fe, Co, Ni, Zn; Ar* = C_6H_3-2,6(C_6H_2-2,4,6-Pr^i_3)$_2$. *J. Am. Chem. Soc.* **2005**, *127*, 8545–8552.

(5) Bürger, H.; Wannagat, U. Silylamido-Derivate von Eisen und Kobalt. *Monatsh. Chem.* **1963**, *94*, 1007–1012.

(6) Bürger, H.; Wannagat, U. Silylamido-Verbindungen von Chrom, Mangan, Nickel und Kupfer. *Monatsh. Chem.* **1964**, *95*, 1099–1102.

(7) Alyea, E. C.; Bradley, D. C.; Copperthwaite, R. G. Three-co-ordinated transition metal compounds. Part I. The preparation and characterization of tris(bis(trimethylsilyl)amido)-derivatives of scandium, titanium, vanadium, chromium, and iron. *J. Chem. Soc., Dalton Trans.* **1972**, 1580–1584.

(8) Alyea, E. C.; Bradley, D. C.; Copperthwaite, R. G.; Sales, K. D. Three-co-ordinated transition metal compounds. Part II. Electronic spectra and magnetism of tris(bis(trimethylsilyl)amido)-derivatives of scandium, titanium, vanadium, chromium, and iron. *J. Chem. Soc., Dalton Trans.* **1973**, 185–191.

(9) Bradley, D. C.; Copperthwaite, R. G.; Cotton, S. A.; Sales, K. D.; Gibson, J. F. Three-co-ordinated transition metal compounds. Part III. Electron spin resonance studies on tris(bis(trimethylsilyl)amido)-derivatives of titanium, chromium, and iron. *J. Chem. Soc., Dalton Trans.* **1973**, 191–194.

(10) Eller, P. G.; Bradley, D. C.; Hursthouse, M. B.; Meek, D. W. Three coordination in metal complexes. *Coord. Chem. Rev.* **1977**, *24*, 1–95.

(11) Bradley, D. C.; Copperthwaite, R. G.; Extine, M. W.; Reichert, W. W.; Chisholm, M. H. Transition Metal Complexes of Bis(Trimethyl-Silyl)Amine (1,1,1,3,3,3-Hexamethyldisilazane). *Inorg. Synth.* **2007**, *18*, 112–120.

(12) Andersen, R. A.; Faegri, K.; Green, J. C.; Haaland, A.; Lappert, M. F.; Leung, A.-P.; Rypdal, K. Synthesis of bis[bis(trimethylsilyl)amido]iron(II). Structure and bonding in $M[N(SiMe_3)_2]_2$ (M = Mn, Fe, Co): two-coordinate transition-metal amides. *Inorg. Chem.* **1988**, *27*, 1782–1786.

(13) Putzer, M. A.; Neumüller, B.; Dehnicke, K.; Magull, J. Synthese und Kristallstrukturen der Amido-Komplexe $[Na(12\text{-Krone-}4)_2][M\{N(SiMe_3)_2\}_3]$ mit M = Mn, Fe und Co. *Chem. Ber.* **1996**, *129*, 715–719.

(14) Murray, B. D.; Power, P. P. Three-coordinate metal amides of manganese(II) and cobalt(II): synthesis and x-ray structure of the first tris(silylamide) of manganese and the x-ray crystal structures of $[M_2(N(SiMe_3)_2)_4]$ (M = Mn, Co). *Inorg. Chem.* **1984**, *23*, 4584–4588.

(15) Olmstead, M. M.; Power, P. P.; Shoner, S. C. Three-coordinate iron complexes: X-ray structural characterization of the amide-bridged dimers $[Fe(NR_2)_2]_2$ (R = $SiMe_3$, C_6H_5) and the adduct $Fe[N(SiMe_3)_2]_2(THF)$ and determination of the association energy of the monomer $Fe\{N(SiMe_3)_2\}_2$ in solution. *Inorg. Chem.* **1991**, *30*, 2547–2551.

(16) Panda, A.; Stender, M.; Olmstead, M. M.; Klavins, P.; Power, P. P. Reactions of M$\{N(SiMe_3)_2\}_2$ (M = Mn, Fe or Co) with pyridine and 4,4′-bipyridyl: structural and magnetic studies. *Polyhedron* **2003**, *22*, 67−73.

(17) Zadrozny, J. M.; Xiao, D. J.; Atanasov, M.; Long, G.; Grandjean, J.; Neese, F.; Long, J. R. Magnetic blocking in a linear iron(I) complex. *Nat. Chem.* **2013**, *5* (7), 577−581.

(18) Zadrozny, J. M.; Atanasov, M.; Bryan, A. M.; Lin, C.-Y.; Rekken, B. D.; Power, P. P.; Neese, F.; Long, J. R. Slow magnetization dynamics in a series of two-coordinate iron(II) complexes. *Chem. Sci.* **2013**, *4*, 125−138.

(19) Atanasov, M.; Zadrozny; Long, J. R.; Neese, F. A theoretical analysis of chemical bonding, vibronic coupling, and magnetic anisotropy in linear iron(II) complexes with single-molecule magnet behavior. *Chem. Sci.* **2013**, *4*, 139−156.

(20) Lin, P.-H.; Smythe, N. C.; Gorelsky, S. I.; Maguire, S.; Henson, N. J.; Korobkov, I.; Scott, B. L.; Gordon, J. C.; Baker, R. T.; Murugesu, M. Importance of out-of-state spin orbit coupling for slow magnetic relaxation in mononuclear FeII complexes. *J. Am. Chem. Soc.* **2011**, *133*, 15806−15809.

(21) Eichhöfer, A.; Lan, Y.; Mereacre, V.; Bodenstein, T.; Weigend, F. Slow Magnetic Relaxation in Trigonal-Planar Mononuclear Fe(II) and Co(II) Bis(trimethylsilyl)amido Complexes—A Comparative Study. *Inorg. Chem.* **2014**, *53*, 1962−1974.

(22) Lin, W.; Bodenstein, T.; Mereacre, V.; Fink, K.; Eichhöfer, A. Field-Induced Slow Magnetic Relaxation in the Ni(I) Complexes $[NiCl(PPh_3)_2]\cdot C_4H_8O$ and $[Ni(N(SiMe_3)_2)(PPh_3)_2]$. *Inorg. Chem.* **2016**, *55*, 2091−2100.

(23) Werncke, C. G.; Vendier, L.; Sabo-Etienne, S.; Sutter, J.-P.; Pichon, C.; Bontemps, S. Crystal Structure and Magnetic Characterization of Three-Coordinate $[M\{N(SiMe_3)_2\}_2(PCyp_3)]$ Complexes with M = Mn(II), Fe(II), and Co(II) (Cyp = Cyclopentyl). *Eur. J. Inorg. Chem.* **2017**, *2017*, 1041−1046.

(24) Ge, N.; Zhai, Y.-Q.; Deng, Y.-F.; Ding, Y.-S.; Wu, T.; Wang, Z.-X.; Ouyang, Z.; Nojiri, H.; Zheng, Y. Z. Rationalization of single-molecule magnet behavior in a three-coordinate Fe(III) complex with a high-spin state ($S = 5/2$). *Inorg. Chem. Front.* **2018**, *5*, 2486−2492.

(25) Indris, S.; Knapp, M.; Schwarz, B.; Eichhöfer, A. A solvent-free crystal structure of $[Fe\{N(SiMe_3)_2\}_3]$ – synthesis, structure and properties. *Eur. J. Inorg. Chem.* **2021**, *2021*, 951−959.

(26) Bodenstein, T.; Eichhöfer, A. Magnetic anisotropy in trigonal planar Fe(II)bis(trimethylsilyl)amido complexes of the type $[Fe\{N(SiMe_3)_2\}_2L]$ – experiment and theory. *Dalton Trans.* **2019**, *48*, 15699−15712.

(27) Deng, Y.-F.; Han, T.; Wang, Z.; Ouyang, Z.; Yin, B.; Zheng, Z.; Krzystek, J.; Zheng, Y.-Z. Uniaxial magnetic anisotropy of square-planar chromium(II) complexes revealed by magnetic and HF-EPR studies. *Chem. Commun.* **2015**, *51*, 17688−17691.

(28) Lin, C.-Y.; Fettinger, J. C.; Power, P. P. Reversible Complexation of Lewis Bases to Low-Coordinate Fe(II), Co(II), and Ni(II) Amides. *Inorg. Chem.* **2017**, *56*, 9892−9902.

(29) Power, P. P. Stable Two-Coordinate, Open-Shell (d1−d9) Transition Metal Complexes. *Chem. Rev.* **2012**, *112*, 3482−3507.

(30) Day, B. M.; Pugh, T.; Hendriks, D.; Guerra, C. F.; Evans, D. J.; Bickelhaupt, F. M.; Layfield, R. A. Normal-to-Abnormal Rearrangement and NHC Activation in Three Coordinate Iron(II) Carbene Complexes. *J. Am. Chem. Soc.* **2013**, *135*, 13338−13341.

(31) Day, B. M.; Pal, K.; Pugh, T.; Tuck, J.; Layfield, R. A. Carbene Rearrangements in Three-Coordinate N-Heterocyclic Carbene Complexes of Cobalt(II) Bis(trimethylsilyl)amide. *Inorg. Chem.* **2014**, *53*, 10578−10584.

(32) Broere, D. L.-J.; Coric, I.; Brosnahan, A.; Holland, P. L. Quantitation of the THF content in $Fe[N(SiMe_3)_2]_2\cdot x$THF. *Inorg. Chem.* **2017**, *56*, 3140−3143.

(33) Wagner, C. L.; Phan, N. A.; Fettinger, J. C.; Berben, L. A.; Power, P. P. Two-coordinate, late first-row transition metal amido derivatives of the bulky ligand -N(SiPr$^i_3$)Dipp (Dipp = 2,6-diisopropylphenyl): effects of the ligand on the stability of two-coordinate Copper(II) complexes. *Inorg. Chem.* **2019**, *58* (9), 6095−6101.

(34) Stennett, C. R.; Fettinger, J. C.; Power, P. P. Unexpected Coordination Complexes of the Metal Tris-silylamides $M\{N(SiMe_3)_2\}_3$ (M = Ti, V). *Inorg. Chem.* **2020**, *59*, 1871−1882.

(35) Stennett, C. R.; Nguyen, T. H.; Power, P. P. Characterization of the "Absent" Vanadium Oxo $V(=O)\{N(SiMe_3)_2\}_3$, Imido $V(=NSiMe_3)\{N(SiMe_3)_2\}_3$, and Imido-Siloxy $V(=NSiMe_3)(OSiMe_3)\{N(SiMe_3)_2\}_2$ Complexes Derived from $V\{N(SiMe_3)_2\}_3$ and Kinetic Study of the Spontaneous Conversion of the Oxo Complex into Its Imido-Siloxy Isomer. *Inorg. Chem.* **2020**, *59*, 11079−11088.

(36) Kneusels, N.-J. H.; Münzer, J. E.; Flosdorf, K.; Jiang, D.; Neumüller, B.; Zhao, L.; Eichhöfer, A.; Frenking, G.; Kuzu, I. Double donation in trigonal planar iron−carbodiphosphorane complexes – a concise study on their spectroscopic and electronic properties. *Dalton Trans.* **2020**, *49*, 2537−2546.

(37) König, S. N.; Schneider, D.; Maichle-Mössmer, C.; Day, B. M.; Layfield, R. A.; Anwander, R. Divalent transition metal silylamide ate complexes. *Eur. J. Inorg. Chem.* **2014**, *2014*, 4302−4309.

(38) Margraf, G.; Schödel, F.; Sänger, I.; Bolte, M.; Wagner, M.; Lerner, H.-W. An electrochemical and structural study of the iron silylamides $[Fe\{N(SiMe_3)_2\}_2]$ and $[Fe\{N(SiMe_3)_2\}_3]$. *Z. Naturforsch., B: J. Chem. Sci.* **2012**, *67*, 549−556.

(39) Pell, A. J.; Pintacuda, G.; Grey, C. P. Paramagnetic NMR in Solution and the Solid State. *Prog. Nucl. Magn. Reson. Spectrosc.* **2019**, *111*, 1−271.

(40) Pavlov, A. A.; Nehrkorn, J.; Zubkevich, S. V.; Fedin, M. V.; Holldack, K.; Schnegg, A.; Novikov, V. V. A Synergy and Struggle of EPR, Magnetometry and NMR: A Case Study of Magnetic Interaction Parameters in a Six-Coordinate Cobalt(II) Complex. *Inorg. Chem.* **2020**, *59* (15), 10746−10755.

(41) Du, K.; Zemerov, S. D.; Carroll, P. J.; Dmochowski, I. J. Paramagnetic Shifts and Guest Exchange Kinetics in ConFe4-NMetal-Organic Capsules. *Inorg. Chem.* **2020**, *59* (17), 12758−12767.

(42) Grey, C. P.; Dupré, N. NMR Studies of Cathode Materials for Lithium-Ion Rechargeable Batteries. *Chem. Rev.* **2004**, *104* (10), 4493−4512.

(43) Pecher, O.; Carretero-Gonzalez, J.; Griffith, K. J.; Grey, C. P. Materials' Methods: NMR in Battery Research. *Chem. Mater.* **2017**, *29* (1), 213−242.

(44) Middlemiss, D. S.; Ilott, A. J.; Clément, R. J.; Strobridge, F. C.; Grey, C. P. Density Functional Theory-Based Bond Pathway Decompositions of Hyperfine Shifts: Equipping Solid-State NMR to Characterize Atomic Environments in Paramagnetic Materials. *Chem. Mater.* **2013**, *25* (9), 1723−1734.

(45) Clément, R. J.; Pell, A. J.; Middlemiss, D. S.; Strobridge, F. C.; Miller, J. K.; Whittingham, M. S.; Emsley, L.; Grey, C. P.; Pintacuda, G. Spin-Transfer Pathways in Paramagnetic Lithium Transition-Metal Phosphates from Combined Broadband Isotropic Solid-State MAS NMR Spectroscopy and DFT Calculations. *J. Am. Chem. Soc.* **2012**, *134* (41), 17178−17185.

(46) Kim, J.; Middlemiss, D. S.; Chernova, N. A.; Zhu, B. Y. X.; Masquelier, C.; Grey, C. P. Linking Local Environments and Hyperfine Shifts: A Combined Experimental and Theoretical ^{31}P and ^{7}Li Solid-State NMR Study of Paramagnetic Fe(III) Phosphates. *J. Am. Chem. Soc.* **2010**, *132* (47), 16825−16840.

(47) Mondal, A.; Kaupp, M. Quantum-Chemical Study of ^{7}Li NMR Shifts in the Context of Delithiation of Paramagnetic Lithium Vanadium Phosphate, $Li_3V_2(PO_4)_3$ (LVP). *Solid State Nucl. Magn. Reson.* **2019**, *101* (May), 89−100.

(48) Mondal, A.; Kaupp, M. Computation of NMR Shifts for Paramagnetic Solids Including Zero-Field-Splitting and Beyond-DFT Approaches. Application to $LiMPO_4$ (M = Mn, Fe, Co, Ni) and MPO_4 (M = Fe, Co). *J. Phys. Chem. C* **2019**, *123* (13), 8387−8405.

(49) Smiley, D. L.; Goward, G. R. Ex Situ ^{23}Na Solid-State NMR Reveals the Local Na-Ion Distribution in Carbon-Coated Na_2FePO_4F during Electrochemical Cycling. *Chem. Mater.* **2016**, *28* (21), 7645−7656.

(50) Bayer, U.; Bock, L.; Maichle-Mössmer, C.; Anwander, R. A facile route toward ceric silylamide $[Ce\{N(SiHMe_2)_2\}_4]$. *Eur. J. Inorg. Chem.* **2020**, *2020*, 101−106.

(51) Berger, T.; Lebon, J.; Maichle-Mössmer, C.; Anwander, R. $CeCl_3$/*n*-BuLi: Unraveling Imamoto‘s organocerium reagent. *Angew. Chem., Int. Ed.* **2021**, *60*, 15622−15631.

(52) Eichhöfer, A.; Lebedkin, S. 1D and 3D Polymeric Manganese(II) Thiolato Complexes: Synthesis, Structure, and Properties of ${}_{\infty}^{3}[Mn_4(SPh)_8]$ and ${}_{\infty}^{1}[Mn(SMes)_2]$. *Inorg. Chem.* **2018**, *57*, 602−608.

(53) Bryan, A. M.; Long, G. J.; Grandjean, F.; Power, P. P. Synthesis, Spectroscopic Characterization, and Determination of the Solution Association Energy of the Dimer $[Co\{N(SiMe_3)_2\}_2]_2$: Magnetic Studies of Low-Coordinate Co(II) Silylamides $[Co\{N(SiMe_3)_2\}_2L]$ (L = PMe_3, Pyridine, and THF) and Related Species That Reveal Evidence of Very Large Zero-Field Splittings. *Inorg. Chem.* **2013**, *52*, 12152−12160.

(54) Alyea, E. C.; Bradley, D. C.; Copperthwaite, R. G.; Sales, K. D. *J. Chem. Soc., Dalton Trans.* **1973**, 185.

(55) Chilton, N. F.; Anderson, R. P.; Turner, L. D.; Soncini, A.; Murray, K. S. PHI: a powerful new program for the analysis of anisotropic monomeric and exchange-coupled polynuclear d- and f-block complexes. *J. Comput. Chem.* **2013**, *34*, 1164−1175.

(56) Freedman, D. E.; Harman, W. H.; Harris, T. D.; Long, G. J.; Chang, C. J.; Long, J. R. Slow magnetic relaxation in a high-spin iron(II) complex. *J. Am. Chem. Soc.* **2010**, *132*, 1224−1225.

(57) Companion, A. L.; Komarynsky, M. A. Crystal field splitting diagrams. *J. Chem. Educ.* **1964**, *41*, 257−262.

(58) Bendix, J.; Brorson, M.; Schäffer, C. E. Accurate empirical spin-orbit coupling parameters ζ_{nd} for gaseous nd^q transition metal ions. *Inorg. Chem.* **1993**, *32*, 2838−2849.

(59) Boča, R. Zero-field splitting in metal complexes. *Coord. Chem. Rev.* **2004**, *248*, 757−815.

(60) Kahn, O. *Molecular Magnetism*; Wiley-VCH: Weinheim, 1993.

(61) Topping, C. V.; Blundell, S. J. A.C. susceptibility as a probe of low-frequency magnetic dynamics. *J. Phys.: Condens. Matter* **2019**, *31*, 013001.

(62) Benniston, A. C.; Melnic, S.; Turta, C.; Arauzo, A. B.; Bartolomé, J.; Bartolomé, E.; Harrington, R. W.; Probert, M. R. Preparation an properties of calciul(II)-based molecular chain decorated with manganese(II) butterfly-like complexes. *Dalton Trans.* **2014**, *43*, 13349−13357.

(63) Rajnák, C.; Titis, J.; Moncol, J.; Micová, R.; Boca, R. Field-Induced Slow Magnetic Relaxation in a Mononuclear Manganese(II) Complex. *Inorg. Chem.* **2019**, *58*, 991−994.

(64) Uchida, K.; Cosquer, C.; Sugisaki, K.; Matsuoka, H.; Sato, K.; Breedlove, B. K.; Yamashita, M. Isostructural M(II) complexes (M = Mn, Fe, Co) with field-induced slow magnetic relaxation for Mn and Co complexes. *Dalton Trans.* **2019**, *48*, 12023−12030.

(65) Scott, P. L.; Jeffries, C. D. Spin-Lattice Relaxation in Some Rare-Earth Salts at Helium Temperatures; Observation of the Phonon Bottleneck. *Phys. Rev.* **1962**, *127* (1), 32−51.

(66) da Cunha, T. T.; Barbosa, V. M. M.; Oliveira, W. X. C.; Pedroso, E. F.; Garcia, D. M. A.; Nunes, W. C.; Pereira, C. L. M. Field-induced slow magnetic relaxation of a six-coordinate mononuclear manganese(II) and cobalt(II) oxamate complexes. *Inorg. Chem.* **2020**, *59*, 12983−12987.

(67) Carlin, R. L.; Duyneveldt, A. J. *Magnetic Properties of Transition Metal Compounds*; Springer: Berlin, 1977.

(68) Davis, L. J. M.; Heinmaa, I.; Ellis, B. L.; Nazar, L. F.; Goward, G. R. Influence of particle size on solution formation and phase interfaces in $Li_{0.5}FePO_4$ revealed by ^{31}P and ^{7}Li solid state NMR spectroscopy. *Phys. Chem. Chem. Phys.* **2011**, *13*, 5171−5177.

(69) Satterlee, J. D. Fundamental concepts of NMR in paramagnetic systems part II: Relaxation effects. *Concepts Magn. Reson.* **1990**, *2*, 119−129.

(70) Novotný, J.; Jeremias, L.; Nimax, V. P.; Komorovsky, S.; Heinmaa, I.; Marek, R. Crystal and Substituent Effects on Paramagnetic NMR Shifts in Transition-Metal Complexes. *Inorg. Chem.* **2021**, *60*, 9368.

(71) Ott, J. C.; Wadepohl, H.; Enders, M.; Gade, L. H. Taking Solution Proton NMR to Its Extreme: Prediction and Detection of a Hydride Resonance in an Intermediate-Spin Iron Complex. *J. Am. Chem. Soc.* **2018**, *140*, 17413−17417.

(72) Suturina, E. A.; Mason, K.; Geraldes, C. F. G. C.; Chilton, N. F.; Parker, D.; Kuprov, I. Lanthanide-induced relaxation anisotropy. *Phys. Chem. Chem. Phys.* **2018**, *20*, 17676−17686.

(73) Suturina, E. A.; Kuprov, I. Pseudocontact shifts from mobile spin labels. *Phys. Chem. Chem. Phys.* **2016**, *18*, 26412−26422.

(74) Perdew, J. P.; Burke, K.; Ernzerhof, M. Generalized Gradient Approximation Made Simple. *Phys. Rev. Lett.* **1996**, *77*, 3865−3868.

(75) Dovesi, R.; Erba, A.; Orlando, R.; Zicovich-Wilson, C. M.; Civalleri, B.; Maschio, L.; Rerat, M.; Casassa, S.; Baima, J.; Salustro, S.; Kirtman, B. Quantum-mechanical Condensed Matter Simulations with CRYSTAL. *Wiley Interdiscip. Rev.: Comput. Mol. Sci.* **2018**, *8*, e1360.

(76) Cahier, B.; Perfetti, M.; Zakhia, G.; Naoufal, D.; El-Khatib, F.; Guillot, R.; Riviere, E.; Sessoli, R.; Barra, A.-L.; Guihery, N.; Mallah, T. Magnetic Anisotropy in Pentacoordinate NiII and CoII Complexes: Unraveling Electronic and Geometrical Contributions. *Chem. - Eur. J.* **2017**, *23*, 3648−3657.

(77) Becke, A. D. Density-functional thermochemistry. III. The role of exact exchange. *J. Chem. Phys.* **1993**, *98*, 5648−5652.

(78) Zhao, Y.; Truhlar, D. G. The M06 suite of density functionals for main group thermochemistry, thermochemical kinetics, non-covalent interactions, excited states, and transition elements: two new functionals and systematic testing of four M06-class functionals and 12 other functionals. *Theor. Chem. Acc.* **2008**, *120*, 215−241.

(79) Bredow, T.; Gerson, A. R. Effect of exchange and correlation on bulk properties of MgO, NiO, and CoO. *Phys. Rev. B: Condens. Matter Mater. Phys.* **2000**, *61*, 5194−5201.

(80) Reimann, C.; Weber, D.; Lerch, M.; Bredow, T. Non-stoichiometry in Bixbyite-Type Vanadium Sesquioxide. *J. Phys. Chem. C* **2013**, *117*, 20164−20170.

(81) Eichhöfer, A.; Lebedkin, S. 1D and 3D Polymeric Manganese(II) Thiolato Complexes. *Inorg. Chem.* **2018**, *57*, 602−608.

(82) Bryan, A. M.; Long, G. J.; Grandjean, F.; Power, P. P. Synthesis, Spectroscopic Characterization, and Determination of the Solution Association Energy of the Dimer $[Co\{N(SiMe_3)_2\}_2]_2$. *Inorg. Chem.* **2013**, *52*, 12152−12160.

(83) Koziskova, J.; Hahn, F.; Richter, J.; Kozisek, J. Comparison of different absorption corrections on the model structure of tetrakis(\m ∼ 2∼-acetato)-diaqua-di-copper(II). *Acta Chim. Slov.* **2016**, *9* (2), 136−140.

(84) Dolomanov, O. V.; Bourhis, L. J.; Gildea, R. J.; Howard, J. A. K.; Puschmann, H. *J. Appl. Crystallogr.* **2009**, *42*, 339−341.

(85) Sheldrick, G. M. SHELXT - integrated space-group and crystal-structure determination. *Acta Crystallogr., Sect. A: Found. Adv.* **2015**, *71*, 3−8.

(86) Brandenburg, K. *Diamond*, version 2.1d; Crystal Impact GbR, 1996−2000.

(87) *WinXPOW*; STOE & Cie GmbH: Darmstadt, 2000.

(88) Lueken, H. *Magnetochemie*; Teubner, B. G.: Stuttgart, 1999; p 426.

(89) Haberditzl, W. Advances in molecular diamagnetism. *Angew. Chem., Int. Ed. Engl.* **1966**, *5*, 288−323.

(90) Laun, J.; Vilela Oliveira, D.; Peintinger, M. F.; Bredow, T. BSSE-Correction Scheme for Consistent Gaussian Basis Sets of Double- and Triple-Zeta Valence with Polarization Quality for Solid-State Calculations. *J. Comput. Chem.* **2019**, *40*, 2364−2376.

(91) Kresse, G.; Furthmüller, J. Efficient iterative schemes for ab initio total-energy calculations using a plane-wave basis set. *Phys. Rev. B: Condens. Matter Mater. Phys.* **1996**, *54*, 11169−11186.

(92) Kresse, G.; Joubert, D. From ultrasoft pseudopotentials to the projector augmented-wave method. *Phys. Rev. B: Condens. Matter Mater. Phys.* **1999**, *59*, 1758−1775.

(93) Dudarev, S. L.; Botton, G. A.; Savrasov, S. Y.; Humphreys, C. J.; Sutton, A. P. Electron-energy-loss spectra and the structural stability of nickel oxide: An LSDA+U study. *Phys. Rev. B: Condens. Matter Mater. Phys.* **1998**, *57*, 1505−1509.